THE JOURNAL OF PHYSICAL CHEMISTRY C

Article

pubs.acs.org/JPCC

# Ultramicroelectrode Studies of Self-Terminated Nickel Electrodeposition and Nickel Hydroxide Formation upon Water Reduction

Nicole L. Ritzert* and Thomas P. Moffat*

Material Measurement Laboratory, National Institute of Standards and Technology, 100 Bureau Drive, Gaithersburg, Maryland 20899, United States

Supporting Information

**ABSTRACT:** The interaction between electrodeposition of Ni and electrolyte breakdown, namely, the hydrogen evolution reaction (HER) via $H_3O^+$ and $H_2O$ reduction, was investigated under well-defined mass transport conditions using ultramicroelectrodes (UMEs) coupled with optical imaging, generation/collection scanning electrochemical microscopy, and preliminary microscale pH measurements. For 5 mmol/L $NiCl_2$ + 0.1 mol/L NaCl, pH 3.0, electrolytes, the voltammetric current at modest overpotentials, i.e., between −0.6 and −1.4 V vs Ag/AgCl, was distributed between metal deposition and $H_3O^+$ reduction, with both reactions reaching mass transport-limited current values. At more negative potentials, an unusual sharp current spike appeared upon the onset of $H_2O$ reduction that was accompanied by a transient increase in $H_2$ production. The peak potential of the current spike was a function of both $[Ni(H_2O)_6]^{2+}(aq)$ concentration and pH. The sharp rise in current was ascribed to the onset of autocatalytic $H_2O$ reduction, where electrochemically generated $OH^-$ species induce heterogeneous nucleation of $Ni(OH)_2(ads)$ islands, the perimeter of which is reportedly active for $H_2O$ reduction. As the layer coalesces, further metal deposition is quenched while $H_2O$ reduction continues, albeit at a decreased rate as fewer of the most reactive sites, e.g., $Ni/Ni(OH)_2$ island edges, are available. At potentials below −1.5 V vs Ag/AgCl, $H_2O$ reduction is accelerated, leading to homogeneous precipitation of bulk $Ni(OH)_2{\cdot}xH_2O$ within the nearly hemispherical diffusion layer of the UME.

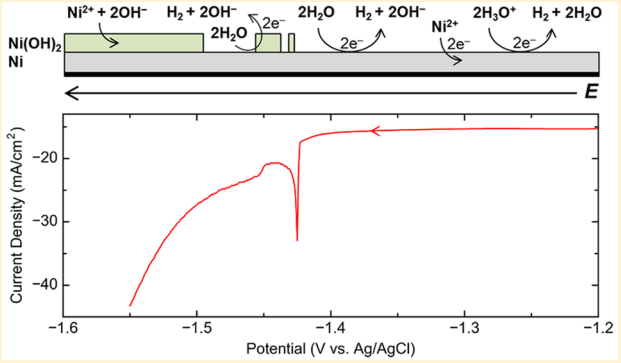


## INTRODUCTION

For many electrodeposition reactions, nucleation and growth is accompanied by electrolyte breakdown that can affect properties such as microstructure, morphology, and chemical composition of the deposit. A prototypical example is the hydrogen evolution reaction (HER), arising from both $H_3O^+$ and $H_2O$ reduction:

$$2H_3O^+ + 2e^- \rightarrow H_2 + 2H_2O \quad (1)$$

$$2H_2O + 2e^- \rightarrow H_2 + 2OH^- \quad (2)$$

The HER occurs during electroplating of iron group elements, e.g., Fe, Co, and Ni, and their alloys. The respective contributions of eqs 1 and 2 depend on the applied potential range. $H_2$ evolution decreases the overall current efficiency of electrodeposition, and the adsorbed H intermediate can be incorporated into the deposit. Under more demanding conditions, i.e., at more negative potentials, the pH at the electrode−electrolyte interface increases, leading to formation of metal hydroxides that competes with metal deposition.[1−11] Thus, to produce metallic films, buffers and complexing agents such as boric acid are commonly added to the electrolyte to mitigate the effects of pH changes.[2,12−14]

The above side reactions have been used to deposit precise nanostructured features and to synthesize electrochemically metal oxides, hydroxides, oxyhydroxides, and their composites. An example of the former is fabrication of ultrathin films of Fe, Co, and Ni on Au through self-terminated metal growth[15] where metal deposition ceases upon the onset of $H_2O$ reduction. This behavior was attributed to the reaction of electrochemically generated $OH^-$ (eq 2) with divalent metal cations to form a hydroxide layer that quenches further metal deposition while supporting continued $H_2O$ reduction. A similar scheme was used to create Ni nanoparticles and fully coalesced thin films on TiN substrates.[16,17] Alternatively, media such as nitrate electrolytes that favor $OH^-$ production have been used to make $Ni(OH)_2$ under well-controlled conditions.[18−20] $Ni(OH)_2$ produced in this manner has been a popular constituent of batteries, electrocatalysts, and supercapacitors[19−23] and is currently receiving renewed interest as a low-dimensional material.[24−26] Of particular relevance to the

Received: October 3, 2016
Revised: November 10, 2016
Published: November 14, 2016




DOI: 10.1021/acs.jpcc.6b10006
J. Phys. Chem. C XXXX, XXX, XXX−XXX

present study is the reported catalytic activity of metal/$Ni(OH)_2$ interfaces toward $H_2O$ reduction.[27−29]

Here, we took advantage of the unique properties of ultramicroelectrodes (UMEs) to investigate further the interplay between metal deposition, the HER, and hydroxide formation with a focus on gaining further insight into the self-terminated electrodeposition of iron group metals in $NiCl_2$−NaCl electrolytes.[15] UMEs generate low currents, allowing for measurements of high current density while minimizing ohmic ($iR$) losses and electrochemical cell $RC$ time constant delays that can distort the current response at macroscale (area of ≈1 $cm^2$) electrodes.[30−33] High mass transport associated with the nearly hemispherical diffusional field of UME disks enables steady-state conditions to be attained readily[30−33] without distortions from forced hydrodynamics that can disturb evolving surface chemistry such as local $H_2O$ structure or gel formation.[34,35] This diffusional field is also more uniform than that associated with free convection at quiescent macroscale electrodes. The dimensions of UMEs are amenable for studying nucleation mechanisms and growth morphology,[31−33,36−42] where the electrode size is commensurate with that of the growing crystals, as well as optical microscopy, where the entire UME area and its diffusion layer can be imaged,[43−47] providing spatial−temporal insight into electrochemical phase transformations. Thus, we took advantage of the optical contrast between Au and Ni to follow the electrodeposition of Ni.

In the following studies with Au UMEs, an unusual voltammetric current spike that can be correlated to self-termination of Ni deposition[15] was observed near the onset of $H_2O$ reduction in $NiCl_2$−NaCl electrolytes. Changes in electrolyte composition as well as generation/collection scanning electrochemical microscopy (G/C-SECM)[48−50] were used to support the hypothesis that the current spike is due to autocatalytic $H_2$ evolution that is associated with the nucleation and growth of a thin nickel hydroxide layer. At more negative potentials and extended $H_2O$ electrolysis, homogeneous precipitation of a $Ni(OH)_2{\cdot}xH_2O$ gel occurred within the electrode diffusion layer, as shown by optical microscopy. Preliminary microscale pH measurements indicated a small pH shift associated with the current spike followed by a more extensive change at more negative potentials.

## EXPERIMENTAL METHODS

Chemicals were used as received. (Commercial materials and equipment are identified in this paper to specify adequately the experimental procedure. In no case does such identification imply recommendation or endorsement by the National Institute of Standards and Technology, nor does it necessarily imply that the product is the best available for the purpose.) Nickel chloride hexahydrate ($NiCl_2{\cdot}6H_2O$, ReagentPlus grade), agar (ash 2.5% to 4.5%), lithium chloride (LiCl, 99. 2% ACS reagent), and sulfuric acid ($H_2SO_4$, 99.999%) were from Sigma-Aldrich (St. Louis, MO). Alfa Aesar (Ward Hill, MA) was the source of cobalt chloride hexahydrate ($CoCl_2{\cdot}6H_2O$, 99.9%), potassium nitrate ($KNO_3$, 99.0% min), nickel sulfate hexahydrate ($NiSO_4{\cdot}6H_2O$, 99.99%), sodium sulfate ($Na_2SO_4$, 99.0% min), and sodium hexachloroiridate (III) hydrate ($Na_3IrCl_6{\cdot}xH_2O$, 31.5% min. Ir). Hydroxymethylferrocene (FcMeOH, 99%) was from Strem Chemicals (Newbury Point, MA). Mallinckrodt (Paris, KY) supplied sodium chloride (NaCl, ACS grade) and boric acid ($H_3BO_3$, ACS grade). Goodfellow Corporation (Oakdale, PA) supplied tempered microwires (99.99%) for fabricating UMEs. Water (18.3 Ω·cm) from an EASYpure UV system (Barnstead-Thermolyne, Dubuque, IA) was used to clean glassware and prepare solutions. All glassware and electrochemical cells were soaked overnight in 3 mol/L $HNO_3$ and then rinsed with copious amounts of water before use. The pH value of electrolyte solutions was 3.0, unless otherwise noted, and was measured using an Oakton Instruments (Vernon Hills, IL) model pH11 meter. Au UMEs with radius, $a$, of 6.25 μm were from CH Instruments (Austin, TX), and those with $a$ = 12.5 μm were from CH Instruments or homemade.[51] Homemade Au UMEs were fabricated by sealing Au wire of diameter, $\phi$, 25 μm in flint glass (i.e., low melting) capillaries in an air/$H_2$ flame. Pt UMEs were made by sealing Pt wire with $\phi$ = 15 or 25 μm in soda-lime capillaries using resistive heating in a pipet puller (Narische Scientific, Tokyo, Japan). Back contact was made with Ag epoxy or eutectic containing a mass fraction of ≈75/25 Ga/In. After the metal disk was exposed with sandpaper of successively finer grit, UMEs were polished with 1.0, 0.3, and then 0.05 μm alumina on polishing cloth. For G/C-SECM, UMEs were sharpened using sandpaper and then polished with alumina. UMEs were characterized in 1 mmol/L FcMeOH + 0.1 mol/L $KNO_3$. In order to define the probe dimensions, experimental approach curves, i.e., plots of tip probe current versus tip−surface separation, at a glass slide were compared to theory for negative feedback current[52] in order to determine the distance of shortest approach between the tip and substrate, $d_0$, and $R_G$ (= $r_g/a$), where $r_g$ is the radius of the glass sheath. $R_G$ ranged from 5 to 10, and $d_0$ ranged from 1 to 2 μm.

Electrochemical measurements were performed at room temperature using a model 920D CH Instruments scanning electrochemical microscope system. At least three repetitions were performed for all measurements. Intervals are reported at the 95% confidence level. Except for optical microscopy measurements, a grounded aluminum Faraday cage on a marble table was used to minimize electronic and vibration disturbances. A graphite rod (spectroscopic grade, Union Carbide, New York, NY) or Ir wire auxiliary electrode was used for all measurements except in SECM, where a Pt wire was used. The reference was an Ag/AgCl/1 mol/L KCl electrode, which was separated from working and auxiliary electrodes by a salt bridge containing 30 g/L agar and 0.2 mol/L $KNO_3$. No effect from trace $NO_3^-$ in the main electrolyte was detected, as results using paper frits were similar to those with salt bridges. Unless noted otherwise, all potentials are reported as ±0.02 V with respect to the Ag/AgCl reference electrode (+0.22 V vs standard hydrogen electrode (SHE)).[53] For cyclic voltammetry and chronoamperometry, electrochemical cells were glass vials of volume 20 mL with plastic lids. Electrodes were introduced through holes cut into the lids. Solutions were deaerated using $N_2$ (zero grade, 99.998%, Roberts Oxygen, Rockville, MD) for at least 20 min prior to each measurement with a blanket of gas always over the solution. Before each measurement, Au UMEs were polished with alumina and then cycled at a sweep rate of 200 mV/s in 0.1 mol/L $H_2SO_4$ between the oxygen (OER) and hydrogen (HER) evolution reactions, viz., between +1.50 V and −0.35 V, respectively. Deposited metal films were removed by immersing the UMEs in 3 mol/L $HNO_3$ for at least 10 min before mechanical polishing.

A PTFE cell of volume 2 mL was used for G/C-SECM measurements. An Au generator UME was used as the moveable tip probe, and a Pt collector UME was used as the stationary substrate electrode. To minimize the amount of dissolved $O_2$, the cell was wrapped with paraffin film containing


DOI: 10.1021/acs.jpcc.6b10006
J. Phys. Chem. C XXXX, XXX, XXX−XXX

a hole large enough to accommodate the tip probe. A Pasteur pipet was used to deaerate the electrolyte for at least 30 min and then blanket the solution with $N_2$. To align the UME disks before running each G/C-SECM measurement, positive feedback current was maximized using the HER at Au and the hydrogen oxidation reaction (HOR) at Pt in 0.1 mol/L NaCl. Positioning error was ±1 μm. After measurements in 0.1 mol/L NaCl, the solution was replaced with 5.0 mmol/L $NiCl_2$ + 0.1 mol/L NaCl while maintaining a constant tip−substrate surface separation, i.e., tip height, *d*.

An Epiphot 300 Metallurgy Inverted Microscope (Nikon, Tokyo, Japan) was used to examine electrodeposited films. For ex situ measurements, the potential was swept or stepped to the desired value in 5 mmol/L $NiCl_2$ + 0.1 mol/L NaCl and then poised for a given time before the UME was removed from solution and rinsed with water. Optical images were obtained using a Polaroid (Minnetonka, MN) model i733 digital camera or a VS8904G smartphone (LG Electronics, Seoul, South Korea) digital camera operating Android 4.4.2 software attached to the side viewing port. For in situ measurements, UMEs were imaged under potential control using a three-electrode cell arrangement. Electrodes were suspended in about 0.25 mL of 5 mmol/L $NiCl_2$ + 0.1 mol/L NaCl on a fused silica plate ($\phi$ = 76 mm, thickness of 0.5 mm, Valley Design East, Shirley, MA) on top of the microscope stage. UMEs were viewed through the bottom of the plate and solution. Images were recorded using a Model OCS-5.0 OptixCam Summit Series CMOS Camera (Microscope Store, LLC, Roanoke, VA) with OCView (version 7.3.1.8) and then processed using ImageJ (version 1.49).[54]

## RESULTS AND DISCUSSION

**Cyclic Voltammetry in 5 mmol/L $Ni^{2+}$ Electrolytes.** The cyclic voltammetry (CV) of Au UMEs in 5.0 mmol/L $NiCl_2$ + 0.1 mol/L NaCl was examined at three reversal potential limits (Figure 1), where the dominant precursor species is $[Ni(H_2O)_6]^{2+}(aq)$,[55,56] although a fraction (<10%) of the nickelous species in 0.1 mol/L NaCl, pH 3.0, may be $[Ni(H_2O)_5Cl]^{-}(aq)$.[56] For simplicity, the discussion will refer to all dissolved nickelous species as $Ni^{2+}$. Upon sweeping negative in the $Ni^{2+}$-free electrolyte (Figure 1, dashed gray line), $H_3O^+$ reduction, reaching mass transport-limited current near −1.0 V, was followed by the onset of $H_2O$ reduction near −1.5 V, as given in eqs 1 and 2, respectively. The half-wave potential of $H_3O^+$ reduction was −0.83 V, far negative of the formal potential of $H_3O^+/H_2$ at −0.40 V vs Ag/AgCl (−0.18 V vs SHE)[57] at pH 3.0, reflecting the poor kinetics of this reaction at Au. In the $Ni^{2+}$ electrolyte (Figure 1, solid gray curve), the increase in the current density, $j_{total}$, at −1.20 V is due to $Ni^{2+}$ reduction, proceeding with concurrent $H_3O^+$ reduction. Ni deposition begins near −0.6 V, corresponding to a small nucleation overpotential relative to the calculated potential of the $Ni^{2+/0}$ couple in 5 mmol/L $Ni^{2+}$ at −0.55 V vs Ag/AgCl (−0.33 V vs SHE).[58] The diffusion coefficients, *D*, of $H_3O^+$ and $Ni^{2+}$ were determined from the steady-state current density, *j*

$$j = 4nFDc\pi^{-1}a^{-1} \quad (3)$$

derived from the steady-state current for a disk UME,[57] where the number of electron equivalents, *n*, is 1 for $H_3O^+$ and 2 for $Ni^{2+}$; *F* is Faraday's constant (96 485 C/mol), and *c* is concentration. The value of $j_{Ni}$ was calculated by subtracting $j_H$ in the supporting electrolyte (Figure 1, dashed gray line) from

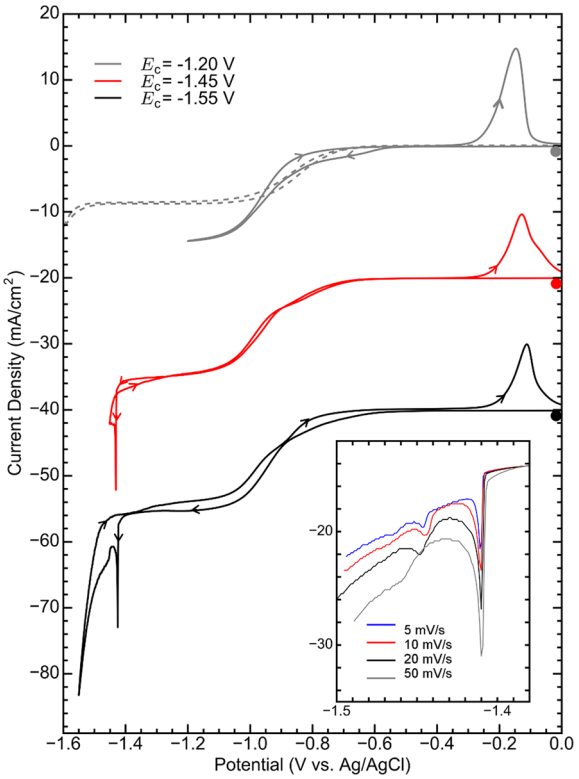


**Figure 1.** Cyclic voltammetry of Au ultramicroelectrode in 5.0 mmol/L $NiCl_2$ + 0.1 mol/L NaCl, pH 3.0, at cathodic reversal potentials, $E_c$, of (gray) −1.20 V, (red) −1.45 V, and (black) −1.55 V. Sweep rate, *v*, 20 mV/s. Gray dashed line is supporting electrolyte. Red and black curves were shifted by −20 and −40 mA/cm$^2$, respectively, for clarity. Inset shows *v* = (blue) 5 mV/s, (red) 10 mV/s, (black) 20 mV/s, and (gray) 50 mV/s, where the potential axis was adjusted so that the peaks were aligned for clarity. Initial potential, 0.00 V; anodic potential limit, 0.00 V; electrode radius, 12.5 μm.

$j_{total}$ in the $Ni^{2+}$ electrolyte (Figure 1, solid gray line) at −1.20 V. Values of $D_H$ and $D_{Ni}$ were (9.5 ± 0.4) × $10^{-5}$ cm$^2$/s and (6.7 ± 0.3) × $10^{-6}$ cm$^2$/s, respectively, corresponding well to literature values of 9.3 × $10^{-5}$ and 6.6 × $10^{-6}$ cm$^2$/s,[59] demonstrating that $H_3O^+$ and $Ni^{2+}$ reduction are well-defined in this potential region. In the reverse sweep, the anodic wave at −0.15 V corresponds to stripping of the Ni film and any incorporated H. The ratio of $j_{Ni}/j_{total}$ at −1.20 V yielded (41 ± 1)% for the current efficiency of $Ni^{2+}$ reduction, whereas the current efficiency was (18 ± 6)% when comparing the charge in the anodic stripping peak to the background-subtracted charge in the deposition wave. Indeed, the $Ni^{2+/0}$ ion-transfer reaction is irreversible,[58] suggesting that only part of the Ni film was removed in the reverse sweep.

When the negative voltammetric limit was extended to −1.45 V (Figure 1, red line), a sharp cathodic spike appeared at an average value of −1.40 V, although in this case, the value was −1.42 V (vide infra). The absence of a corresponding feature in the reverse sweep suggests that this feature was due to an (electro)chemically irreversible process. The rapid increase in current density is suggestive of a two-dimensional heterogeneous nucleation and growth process in which growing deposited islands give rise to an increased electrochemically active surface area followed by a decay in current during coalescence.[32,36,60] Furthermore, for 10 replicate measurements at pH 3.0, the potential of the peak appeared anywhere between


DOI: 10.1021/acs.jpcc.6b10006
J. Phys. Chem. C XXXX, XXX, XXX−XXX

−1.44 V and −1.38 V, indicating that this process is highly sensitive to the electrode surface and possibly reflects the stochastic nature of nucleation. The peak was more pronounced, i.e., the peak current density was higher and the current rise occurred within 2 mV, at electrodes that had been pretreated electrochemically by cycling through Au oxide formation when compared to those cleaned with only mechanical polishing.

Reduction of both $Ni^{2+}$ and $H_3O^+$ was under mass transport conditions at −1.40 V, precluding them as the source of a nucleation-induced current spike, whereas the spike occurs just after the onset of $H_2O$ reduction. A reasonable hypothesis is that the $OH^-$ generated at the electrode surface via $H_2O$ reduction reacts with the inward diffusing $Ni^{2+}$ to form a thin nickel hydroxide layer, which will be referred to as Ni-$(OH)_2$(ads) for simplicity. The solubility product constant, $K_{sp}$, for homogeneous precipitation of $Ni(OH)_2$, $\approx 10^{-16}$ $mol^3/L^3$,[61−64] is exceeded at 5 mmol/L $Ni^{2+}$, and the electrode surface may further stabilize a heterogeneous thin $Ni(OH)_2$ layer. Recent work on $H_2$ evolution in alkaline media reveals that composite $Ni/Ni(OH)_2$ surfaces are more catalytic than bare Ni toward water reduction.[28] Thus, the interaction between $Ni^{2+}$ and electrochemically generated $OH^-$ may lead to autocatalytic water reduction and further $Ni(OH)_2$(ads) formation at the boundary between $Ni(OH)_2$(ads) nuclei and Ni. Accordingly, the $H_2O$ reduction activity rises sharply with $Ni(OH)_2$(ads) island nucleation and perimeter expansion followed by a decay in current as the film coalesces and the number of $Ni/Ni(OH)_2$(ads) active sites decreases. Substitution of LiCl for the NaCl supporting electrolyte did not enhance the $H_2O$ reduction kinetics (Figure S1), in contrast to recent studies of water reduction at $Pt/Ni(OH)_2$ electrodes.[27]

Coincident with potentials where the current spike occurs, Ni deposition was quenched in previous electrochemical quartz crystal microbalance (EQCM) measurements at macroscale (area of ≈1 $cm^2$) electrodes in 5.0 mmol/L $NiCl_2$ + 0.1 mol/L NaCl, pH 3.0.[15] However, in contrast to UME measurements, only a small wave was evident, possibly due to the more uniform diffusion field and higher flux of material at UMEs. The lower potential of the wave marked not only the onset of quenching of the Ni deposition reaction but also an increase in EQCM dissipative losses that was ascribed to increased hydrogen bonding between the nickel hydroxide layer and the electrolyte. At the terminus of the voltammetric wave, metal deposition was blocked by a fully formed hydroxide layer while $H_2O$ reduction was sustained below −1.5 V.

At a more negative potential limit of −1.55 V (Figure 1, black line), another smaller, broader peak occurred negative of the current spike. More peaks were revealed at slower potential sweep rates (inset of Figure 1), indicating a secondary process such as hydrolysis (vide infra). Results for Ni deposition on Pt UMEs (Figure S2) produced a similar current spike and subsequent waves, indicating that these processes are insensitive to the underlying substrate electrode. The half-wave potential of $H_3O^+$ shifted negative by about 0.6 V in the reverse sweep, confirming that Ni dominates the observed electrochemical behavior.

To understand better the role of the supporting electrolyte, Ni deposition was examined in 5.0 mmol/L $NiSO_4$ + 0.05 mol/L $Na_2SO_4$ (Figure S3). A current spike appeared at −1.46 V, indicating that anions in the supporting electrolyte are not central to the phenomenon. In some cases, a second wave was observed at more negative potentials, reflecting the variability in electrode preparation (vide supra). The higher current on the diffusion-limited plateau in the supporting electrolyte relative to that in the chloride electrolyte may be due to dissociation of bisulfate anions, $pK_a$ = 1.99,[65] in the $H_3O^+$-depleted diffusion layer. In addition to sulfate, borate is a common additive in Ni plating baths used to stabilize deposition by preventing formation of nickel hydroxide species.[12−14] Voltammetry performed in 5.0 mmol/L $NiCl_2$ + 0.05 mol/L NaCl + 0.05 mol/L $H_3BO_3$, pH 3.0 (Figure S4) revealed a current peak at −1.51 V, negative of the spike in $NiCl_2$−NaCl media and further past the onset of $H_2O$ reduction. Thus, nucleation of $Ni(OH)_2$(ads) appears to be delayed in the $NiCl_2$−NaCl−$H_3BO_3$ electrolyte. Production of metallic Ni films in borate media has traditionally been attributed to buffering action, but no significant change in the transport-limited $H_3O^+$ reduction current is evident. Alternatively, borate adsorption or even polyborate formation on the surface may hinder or block $Ni(OH)_2$(ads) formation,[6,66] although investigation of this hypothesis lies beyond the objectives of the present work.

The peak shape of the spike was similar for sweep rates from 5 to 50 mV/s in the $NiCl_2$−NaCl electrolyte (inset of Figure 1) in that the peak current density was reached within 2 mV of its onset. However, no systematic change in the peak potential with sweep rate was detected, likely due to the dispersion associated with surface preparation (vide supra). For sweep rates of 10 and 20 mV/s (Figure S5), the relationship between the postpeak decaying current density and $t^{-1/2}$ was linear when $t$ was less than 1 s, possibly reflecting the decrease in the number of $Ni/Ni(OH)_2$ sites. However, it should be noted that such time-dependent analysis is an approximation because steady-state conditions are often achieved within ≈100 ms at UMEs.[57] The charge in the current spike, calculated by integrating the current between the foot of the spike and the inflection point before the second feature, was (8.7 ± 2.1), (8.8 ± 1.3), (4.7 ± 0.7), and (2.7 ± 0.5) $mC/cm^2$ at sweep rates of 5, 10, 20, and 50 mV/s, respectively, decreasing with increasing sweep rate. The charge was two orders of magnitude larger than the 0.1 $mC/cm^2$ observed in the corresponding feature at macroelectrodes, likely reflecting the more uniform mass transport and higher mixing rate of reactants to and from the UMEs.[37,67,68] The relationship between the peak current density and sweep rate is nonlinear, and the charge is over ten times larger than 0.2 $mC/cm^2$, the surface coverage expected for a monolayer of $Ni(OH)_2$, based on $n$ = 2 for the Ni and $1.06 \times 10^{-9}$ $mol/cm^2$ for $3Ni(OH)_2 \cdot 2H_2O$.[69] Thus, this feature is not due to reduction of a simple adsorbed species such as $Ni(OH)_2$.

Examination of the stripping wave in Figure 1 revealed how $H_2O$ reduction affected the deposited Ni metal film. Compared with results using a reversal potential limit of −1.20 V, the stripping peak shifted positive for both potential negative limits of −1.45 and −1.55 V, and the integrated charge was smaller, suggesting that $H_2O$ reduction is associated with formation of a passivating layer. Voltammetry collected using a more negative potential limit would be expected to yield a larger stripping wave as more Ni would be deposited. However, formation of a passivating nickel hydroxide layer could lead to less subsequent Ni metal deposition as well as inhibition of its dissolution during the reverse sweep. $Ni^{2+}$ reduction seemed to occur during the reverse sweep, as the current density at −1.20 V is similar in both sweep directions, but it is unclear if metal deposition occurred. Further analysis of the stripping peak is beyond the scope of this discussion.



DOI: 10.1021/acs.jpcc.6b10006
J. Phys. Chem. C XXXX, XXX, XXX−XXX

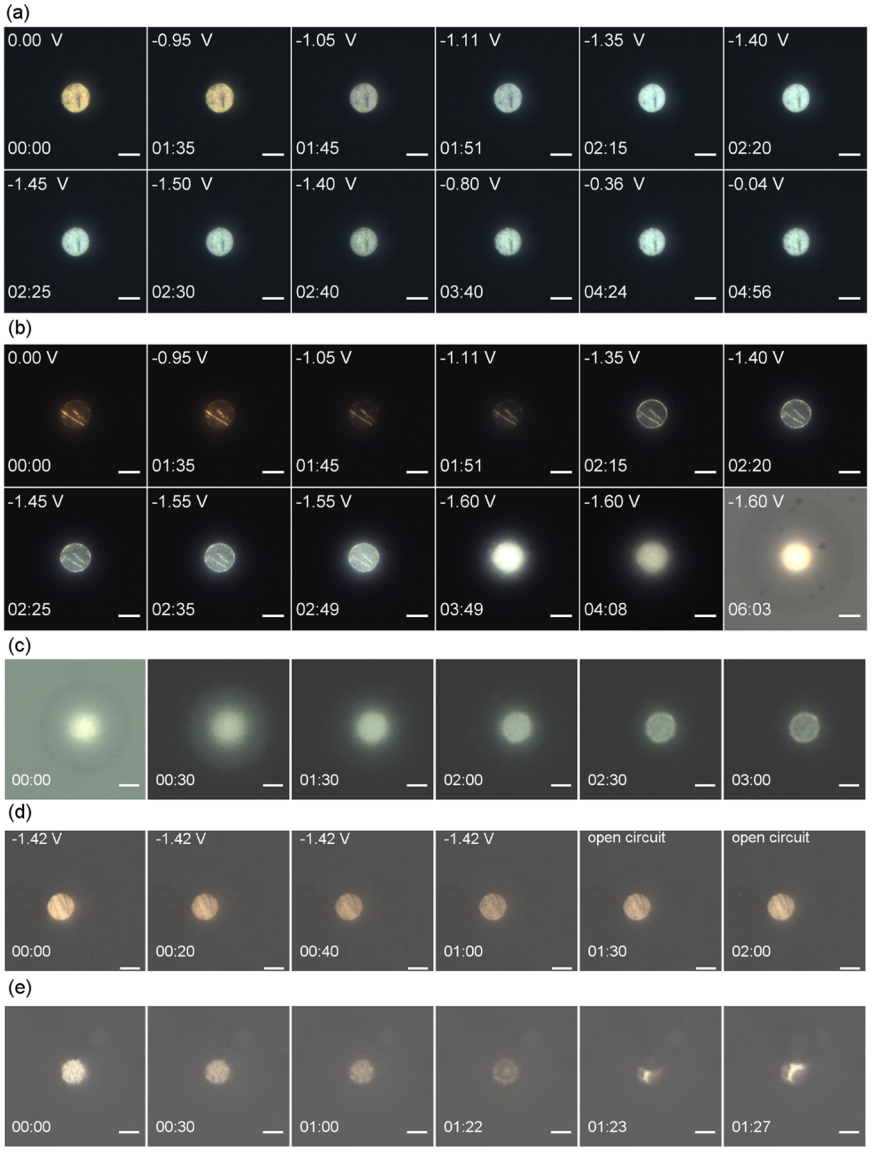


**Figure 2.** Individual frames from optical microscopy of Au ultramicroelectrodes in 5 mmol/L $NiCl_2$ + 0.1 mol/L NaCl corresponding to (a) Video S1, (b) Video S2, (c) Video S3, (d) Video S4, and (e) Video S5. (a) Brightfield and (b) darkfield images (last image is brightfield) during cyclic voltammetry; sweep rate, 10 mV/s; initial potential, 0.00 V. (c) Darkfield images (first image is brightfield) at open circuit after poising potential at −1.60 V for 180 s. (d, e) Brightfield images during chronoamperometry, where $E$ = −1.42 V at bare Au (d) and −1.55 V at Au/Ni (e), deposited at −1.20 V for 60 s. Images were collected at (a−c) 1 frame/s and (d, e) 5 frames/s. Applied potential and time in minutes:seconds (min:s) are labeled in upper and lower left corners, respectively. Electrode radius, 12.5 $\mu$m; scale bar, 20 $\mu$m.

Variation of the size and shape of the UME enhanced the magnitude of the current spike. Poising the potential of the UME for 3 min at −1.20 V before continuing to sweep negative (Figure S6) resulted in a rough overgrowth of Ni beyond the Au disk, with $a$ increasing by ≈3 $\mu$m based on the ratio of $j_{total}$ before and after the potential hold. The spike still occurred upon continuing the negative scan, demonstrating that the spike is not due to growth instability such as a sudden increase in electrode area. In this case, the peak current density increased by a factor of five, perhaps due to roughening of the overgrowth. Simply increasing the electrode area is unlikely the cause of the larger peak current density because performing the experiment with freshly prepared $a$ = 6.25 $\mu$m UMEs produced a larger spike current density as well. In Figure S7, the current response at Au UMEs with $a$ = 6.25 $\mu$m is compared with that at 12.5 $\mu$m UMEs in 5.0 mmol/L $NiCl_2$ + 0.1 mol/L NaCl, pH 2.8. At −1.20 V, the current density at the 6.25 $\mu$m UMEs was nearly twice that of the $a$ = 12.5 $\mu$m UMEs, as expected, because steady-state current density at a disk UME is inversely proportional to $a$ (eq 3). The integrated peak charge of (9.2 ± 3.1) mC/cm$^2$ at the 6.25 $\mu$m UMEs also doubled when compared to (3.8 ± 1.9) mC/cm$^2$ at the 12.5 $\mu$m UMEs, demonstrating that the spike does not scale in proportion with electrode area, as would be expected for reduction of a simple adsorbed species such as $Ni(OH)_2$ (vide supra). Enhanced deposition due to higher $Ni^{2+}$ flux at the electrode edge will lead to the development of a convex edge shape, and at longer times, the electrode will evolve toward a hemispherical shape. This shape evolution will occur more rapidly at the smaller UMEs, leading to improved uniformity of the current distribution compared to that at a disk.


DOI: 10.1021/acs.jpcc.6b10006
J. Phys. Chem. C XXXX, XXX, XXX−XXX

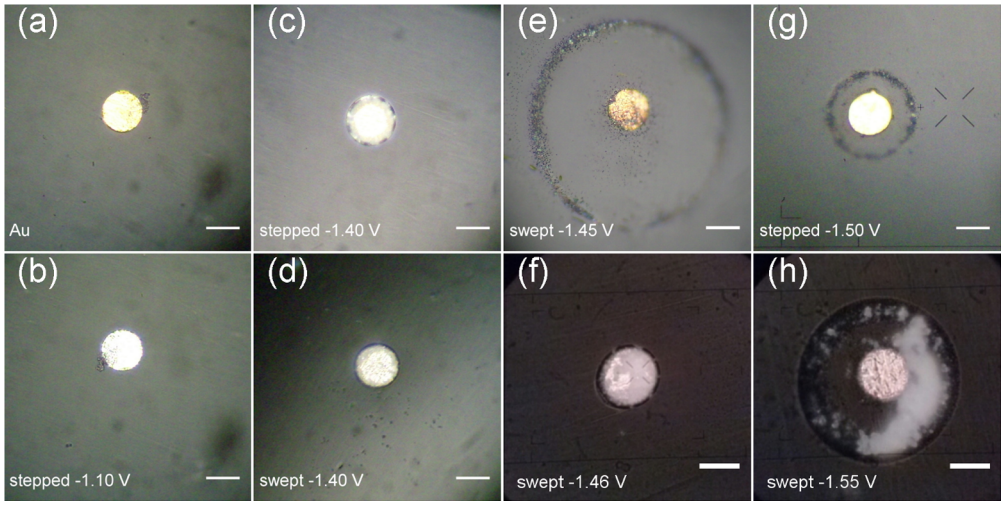


**Figure 3.** Optical microscopy of Ni electrodeposited by linear sweep voltammetry (swept) or chronoamperometry (stepped) at Au ultramicroelectrodes in 5 mmol/L $NiCl_2$ + 0.1 mol/L NaCl: (a) bare Au; (b) swept to −1.10 V and poised 120 s; (c) stepped to −1.40 V for 60 s; (d) swept to −1.40 V and poised 120 s; (e) swept to −1.45 V and poised 60 s; (f) swept to −1.46 V and poised 120 s; (g) stepped to −1.50 V for 60 s; (h) swept to −1.55 V and poised 120 s. For voltammetry: sweep rate, 20 mV/s; initial potential, 0.00 V. Electrode radius, 12.5 $\mu$m; scale bar, 20 $\mu$m.

**Optical Microscopy in 5 mmol/L $NiCl_2$ + 0.1 mol/L NaCl.** The surface and surrounding diffusion layer of Au UMEs were monitored during Ni electrodeposition using optical microscopy. Videos compiled from sequences of still images and their corresponding voltammograms (Figure S8) and descriptions are given in the Supporting Information, with highlights from each sequence in Figure 2. Darkfield imaging, where scattered light provides contrast,[70] revealed additional features, viz., formation of a gray gel, obscured in the brightfield. As the potential was swept to −1.20 V (Videos S1 and S2; Figure 2a,b), smooth, bright Ni films deposited, as expected. No definitive optical changes such as bulk precipitation and $H_2$ bubbles were evident at potentials of about −1.40 V, corresponding to the cathodic spike. In addition, the smooth current response in the voltammetry contrasts with the noisy current associated with $Cr(OH)_3(s)$ precipitation in $Cr^{3+}$ electrolytes[71] and the sharp decrease in the current upon generation of $H_2$ bubbles.[72] However, image processing by taking the difference between the image at −1.25 V and images collected between −1.26 V and −1.50 V in Video S2 suggests that the spike is accompanied by a subtle optical change near −1.37 V (Figure S9). The increase in brightness at the electrode edge during diffusion-limited reduction of $Ni^{2+}$ (Video S2; Figure 2b) reflects enhanced electrodeposition due to higher $Ni^{2+}$ flux.[32,73] At potentials negative of the spike near −1.40 V (Videos S1 and S2; Figure 2a,b), the electrode surface gradually appeared more granular. Homogeneous precipitation of bulk $Ni(OH)_aCl_{2-a}{\cdot}xH_2O$, which will be referred to as $Ni(OH)_2{\cdot}xH_2O$, and the resulting change in optical density could perturb the light path from the electrode surface; indeed, at extended times at −1.50 to −1.60 V, a circular, light gray gel formed, with a larger diameter at higher overpotentials (Video S2; Figure 2b). The gel subsequently dissipated over time under open-circuit conditions (Video S3; Figure 2c). The distance between the edge of the gel and the Au disk was tens of micrometers, corresponding well to the expected thickness of the nearly hemispherical diffusion layer at UMEs.[57]

The evolution of the UME surface was also examined during potential steps, i.e., chronoamperometry. A more detailed analysis of current transients in $Ni^{2+}$ electrolytes is given in the Supporting Information (Figure S10). In Video S4 and Figure 2d, stepping to −1.42 V revealed little change in the reflectivity of the Au electrode at short times, consistent with self-terminated growth of ultrathin Ni films.[15] After 20 s, the reflectivity decreased slightly, although the color of the underlying Au electrode was still apparent. This change is likely due to formation of a $Ni(OH)_2{\cdot}xH_2O$ gel which dissipates over time under open-circuit conditions, similar to Video S3 and Figure 2c. In a related experiment, after Ni was deposited at −1.20 V for 60 s, the potential was stepped to −1.55 V (Video S5; Figure 2e), resulting in rapid coverage of the electrode surface with a gel that densified with time. After 83 s, $H_2$ gas evolution disrupted the gel, and part of the Ni layer was removed, exposing the underlying Au electrode, similar to the peeling of Au thin films during the HER at high overpotentials.[74] Similarly, in some voltammetric studies, $H_2$ bubbles were observed at extended times while poising the potential below −1.5 V.

Some of the modified electrodes were removed from solution, rinsed with water, and compared with bare Au (Figure 3a). Note that these films can be altered upon removal from the deposition electrolyte. Smooth, bright Ni films were deposited at −1.10 V (Figure 3b), as expected. At potentials near the spike (Figure 3c,d), the Ni film had metallic rings at the UME edge as a result of the enhanced deposition rate at the perimeter of the electrode, as seen in Video S2. The Ni film exhibited a variety of morphologies when $H_2O$ reduction takes place. Gray rings with a diameter larger than the UME usually formed on the glass sheath that surrounds the electrode (Figure 3e,g,h). Similarly, rings were observed during precipitation of Prussian blue species caused by Co dissolution from a SECM tip, where the rings defined the edge of the diffusion layer.[75] In the present work, the rings are likely remnants of the $Ni(OH)_2{\cdot}xH_2O$ gel. Some of them were iridescent, congruent with the color changes reported for $Ni(OH)_2$ precipitation at macroelectrodes.[7,18] The metallic parts in the ring and the exposed underlying Au could be part of the damaged Ni film lifted away from the Au surface during the HER (Figure 2e). Differences in


DOI: 10.1021/acs.jpcc.6b10006
J. Phys. Chem. C XXXX, XXX, XXX−XXX

the appearance at similar potentials in Figure 3e,f were likely due to variations in electrode preparation and precise potential of the spike (vide supra). During the potential step to −1.50 V (Figure 3g), the apparently bare Au disk is consistent with self-terminated deposition of an ultrathin Ni film.

Scanning electron microscopy (SEM) and energy dispersive X-ray spectroscopy (EDX) (Figure S11) on a sample swept to −1.55 V confirmed that the ring contains Ni. Raman spectra (Figure S12; Table S1) were collected at various regions of a similarly treated sample. For reference, spectra from a Ni layer grown at −1.20 V are also shown. Comparison to literature[76] shows that peaks at 451, 1388, 1434, 1604, and 3639 $cm^{-1}$ are congruent with $Ni(OH)_2$ on the metallic parts, gray ring, and apparently bare Au.

**Effect of $Ni^{2+}$ Concentration and pH.** The concentration of $Ni^{2+}$, $c_{Ni}$, was varied from 1 to 25 mmol/L (Figure 4a), and the pH of the supporting electrolyte was varied from 2.6 to 4.5 (Figure 4b), where the main nickelous species is $[Ni(H_2O)_6]^{2+}(aq)$.[55,56,62,63] The lower and upper pH values were chosen to avoid generation of $H_2$ bubbles and precipitation of $Ni(OH)_2{\cdot}xH_2O$ in the bulk electrolyte, respectively. The current efficiency at −1.20 V increased from (41 ± 1)% to (81 ± 2)% as the $Ni^{2+}$ concentration was increased from 5.0 to 25.0 mmol/L. Likewise, for 5 mmol/L $Ni^{2+}$, the metal deposition efficiency increased from (17 ± 7)% at pH 2.8 to (96 ± 0.3)% at pH 4.5. The contribution from the HER decreases in both cases as $c_{Ni}$ and pH increase. The current spike at 1 mmol/L $Ni^{2+}$ was broader than that in more concentrated solutions, suggesting that the sharpness of the peak is limited by flux of $Ni^{2+}$. Here, few, disperse $Ni(OH)_2$(abs) islands form before bulk $H_2O$ reduction takes place, similar to the reported low efficiency of $Ni(OH)_2$ deposition at low $Ni(NO_3)_2$ concentrations.[18] The magnitude of the current spike decreases as $c_{Ni}$ and pH increase, suggesting that the hydroxide layer coalesces at a much faster rate with a higher flux of reactants. The positive shift in potential with increasing $c_{Ni}$ is expected from thermodynamics of $Ni(OH)_2$ formation. The slopes of the average peak current potential versus $\log_{10}(c_{Ni})$ and the peak potential versus pH were +230 mV/log $c_{Ni}$ and +110 mV/pH unit, respectively, indicating a complicated mechanism for $Ni(OH)_2$ formation. The positive slope in the latter case suggests that $OH^-$ participates as a reactant. Regardless of a detailed mechanism, these results show that the process giving rise to the spike clearly depends on both $Ni^{2+}$ and pH.

**HER at Au/Ni in Supporting Electrolyte.** Figure 5 shows the voltammetric behavior of Au/Ni in 0.1 mol/L NaCl in the absence of $Ni^{2+}$ along with the results in $NiCl_2$−NaCl electrolyte from Figure 1, comparing the kinetics of $H_2O$ reduction at Ni electrodeposited at different potentials. Full voltammograms are given in Figure S13 along with the detailed deposition experimental procedure. The current spike was absent in all cases, confirming that this feature depends on the presence of $Ni^{2+}$. At a deposition potential of −1.20 V (Figure 5, red curve) to form Au/Ni, the onset of $H_2O$ reduction occurred near −1.35 V, 0.15 V positive of that at Au. This potential was similar to that of the current spike, indicating that the spike begins just after the onset of $H_2O$ reduction at an Au/Ni film. Indeed, the foot of the current spike in Figure 1 exhibited a smooth rise from the diffusion-limited plateau of $H_3O^+$ and $Ni^{2+}$ reduction before the sharp acceleration in current. The first and fifth cycles nearly overlap, demonstrating that any oxidation of Ni during transfer of the UME from the

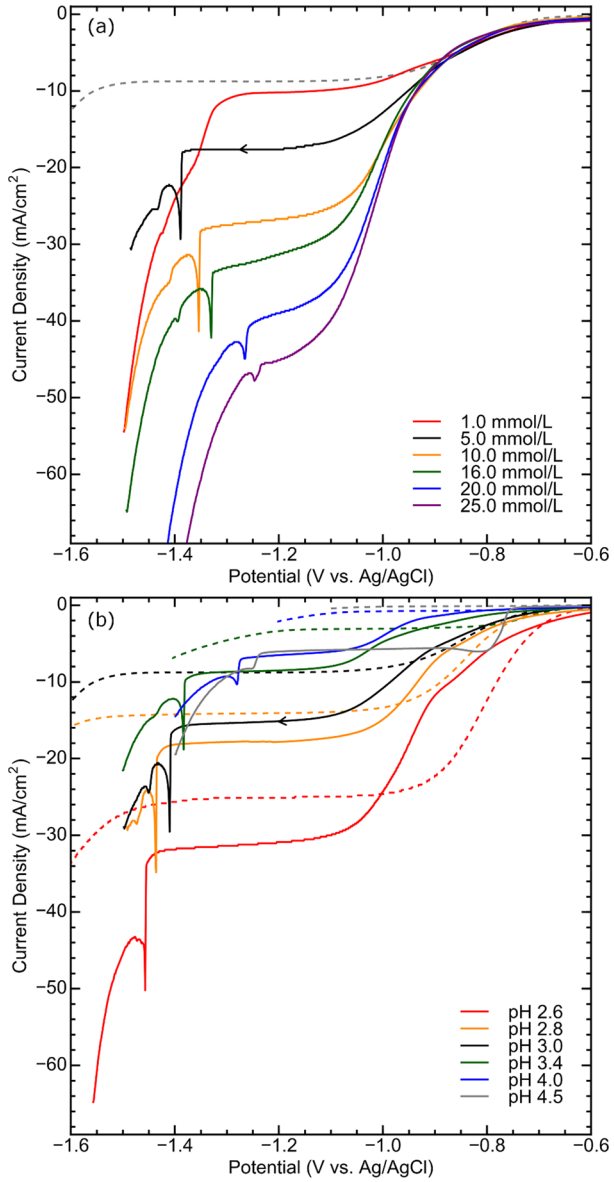


**Figure 4.** Linear sweep voltammetry with varying (a) concentration of $Ni^{2+}$, $c_{Ni}$, and (b) pH. In panel a, $c_{Ni}$ was (red) 1.0 mmol/L, (black) 5.0 mmol/L, (orange) 10.0 mmol/L, (green) 16.0 mmol/L, (blue) 20.0 mmol/L, and (purple) 25.0 mmol/L $NiCl_2$ in 0.1 mol/L NaCl, pH 3.0. In panel b, $c_{Ni}$ was 5.0 mmol/L, and the pH of the 0.1 mol/L NaCl was (red) 2.6, (orange) 2.8, (black) 3.0, (green) 3.4, (blue) 4.0, and (gray) 4.5. Initial potential, 0.00 V; sweep rate, 20 mV/s; electrode radius, 12.5 μm. Dashed lines are the corresponding supporting electrolyte at bare Au.

$Ni^{2+}$ electrolyte does not exert a large effect on $H_2O$ reduction kinetics. For films deposited at −1.47 and −1.55 V (Figure 5, gray and blue curves, respectively), the onset of $H_2O$ reduction shifted positive to about −1.2 V during the first cycle, indicating that this surface is more active for $H_2O$ reduction than Au or Au/Ni, perhaps due to formation of a catalytic Ni/$Ni(OH)_2$ film.[27−29] However, by the third cycle, the potential shifted negative to −1.35 V, possibly due to deactivation or delamination of the active species.

**Collection of $H_2$ Using SECM.** G/C-SECM was used to detect $H_2$ produced during Ni electrodeposition with a focus on contributions associated with the current spike (Figure 6). Although more sensitive measurements can be made with


DOI: 10.1021/acs.jpcc.6b10006
J. Phys. Chem. C XXXX, XXX, XXX−XXX

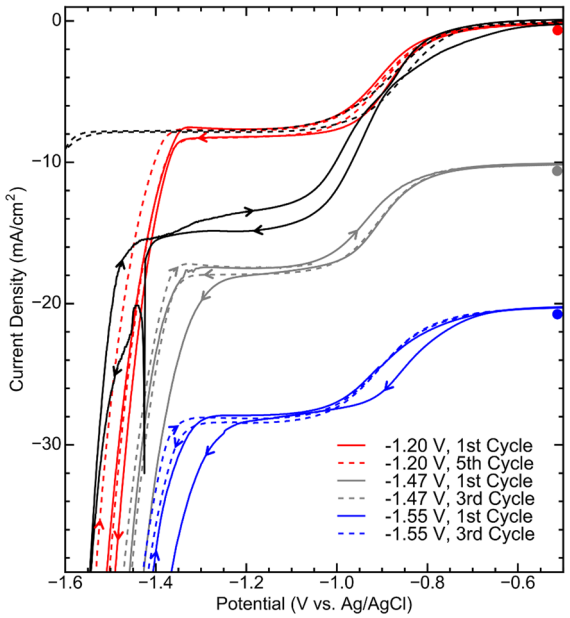


**Figure 5.** Cyclic voltammetry of Au/Ni in 0.1 mol/L NaCl, pH 3.0, in the absence of $Ni^{2+}$. Deposition potential of Ni was (red) −1.20 V, (gray) −1.47 V, and (blue) −1.55 V in 5.0 mmol/L $NiCl_2$ + 0.1 mol/L NaCl. Dashed black line is bare Au, solid lines first cycle of Au/Ni, and dashed lines (red) fifth and (gray, blue) third cycle of Au/Ni. Gray and blue curves were shifted by −10 and −20 mA/cm$^2$, respectively. Sweep rate, 20 mV/s; initial potential, − 0.50 V; electrode radius, 12.5 $\mu$m. Solid black line is the $NiCl_2$−NaCl electrolyte for comparison.

smaller electrode separations, preliminary measurements showed that the flux of $Ni^{2+}$ to the Au was hindered when the separation was less than ≈10 $\mu$m, resulting in more limited Ni deposition. The Pt collector UME was poised at 0.00 V to oxidize any $H_2$ while the potential of the Au generator UME was swept negative. Current collection efficiency, defined as the ratio $j_{Pt}/j_{Au}$, where $j_{Pt}$ and $j_{Au}$ are the current densities at the Pt collector and Au generator electrodes, respectively, is given over the potential range of −0.5 V to −1.5 V in Figure 6b. The more positive potential onset of −0.4 V for $H_3O^+$ reduction (Figure 6a) compared to that in Figure 1 could be due to trace Pt contamination from dissolution of the auxiliary electrode.[77] The current collection efficiency for $H_3O^+$ reduction was (54 ± 8)% at −1.20 V in the supporting electrolyte. A similar value of 55% was obtained for FcMeOH in a similar configuration, indicating that little of the H intermediate in the former experiment is absorbed by the Au substrate. When the supporting electrolyte was replaced with 5.0 mmol/L $NiCl_2$ + 0.1 mol/L NaCl, a broad feature appeared between −0.55 and −0.85 V, attributed to catalyzed $H_3O^+$ reduction at a Pt-contaminated surface.[77] Similar to deposition at Pt UMEs (Figure S2), the inflection at −0.85 V suggests that $H_3O^+$ reduction was inhibited following the onset of Ni deposition. The downward slope in the current plateau from −1.10 to −1.40 V may be due to complicated mass transport in the gap, where $H_3O^+$ exhibits positive feedback and the $Ni^{2+}$ flux is constrained by cylindrical diffusion. Here, the lower collector current compared to that in the supporting electrolyte may be attributed to incorporation of the H intermediate in the growing deposit. An estimate of the concentration of H incorporated in Ni deposited at −1.20 V can be derived by partitioning the partial current for diffusion-limited $H_3O^+$ reduction (Figure 1) by the ratio of the SECM collector

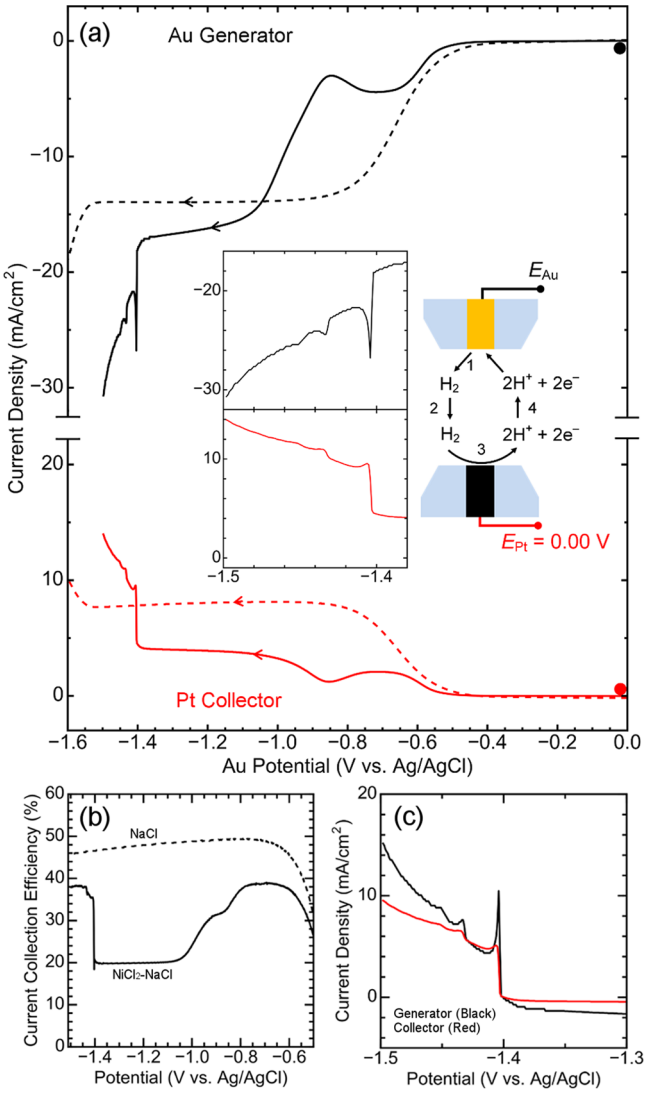


**Figure 6.** Generation/collection mode of scanning electrochemical microscopy in 5.0 mmol/L $NiCl_2$ + 0.1 mol/L NaCl, pH 3.0. (a) Potential of Au generator (black) was swept while potential of Pt collector (red) was poised at 0.00 V. Dashed lines are in the absence of $Ni^{2+}$. Inset shows expanded view of features near $H_2O$ reduction. Diagram shows $H_2$ (1) generated at Au (2) diffusing to Pt collector (3) then being oxidized to protons, which can (4) diffuse back to Au. Electrode separation, 16 $\mu$m; sweep rate, 10 mV/s; initial potential, 0.00 V; electrode radii, 12.5 $\mu$m. (b) Current collection efficiency as a function of potential. Solid and dashed lines are for the $Ni^{2+}$ electrolyte and supporting electrolyte, respectively. (c) Overlaid plots of the magnitude of the current density of (black) Au generator and (red) Pt collector near $H_2O$ reduction, with the foot of the wave set to zero. Note that the potential axis is different in each panel.

currents in Figure 6a. Such analysis yields a deposit stoichiometry close to $Ni_3H$ for films grown on an unobstructed UME.

The current spike was clearly observed at −1.40 V, followed by smaller, broader waves, consistent with the UME experiments in Figure 1. A corresponding spike and waves appeared at the Pt collector, confirming that these features involve the HER. Comparison of the magnitude of the peak heights between Au and Pt in Figure 6c shows that the peak current collection efficiency was nearly 50%, consistent with the current spike being ascribed to HER. Because $H_3O^+$ is transport-limited


DOI: 10.1021/acs.jpcc.6b10006
J. Phys. Chem. C XXXX, XXX, XXX−XXX

at this potential, $H_2O$ reduction was the source of $H_2$. Compared with the mass transport-limited region from −1.10 to −1.40 V (Figure 6b), the nominal current collection efficiency increased sharply by 18% upon the current spike, returning to the original value of 38% before Ni deposition, consistent with the termination of the Ni deposition reaction and negligible further H incorporation into the deposit.

The charge in the current spike at Au was (5.2 ± 1.1) mC/cm$^2$, agreeing well with the value from Figure 1. This value was calculated by integrating from the foot of the spike to the inflection point before the second wave, using the same potential range for the Au and Pt current responses. The charge collection efficiency, (79 ± 7)%, was determined by dividing the charge at Pt by that at Au. When the integration limits were expanded from the foot of the spike to the inflection point following the last wave in order to include the entire postspike feature, the charge collection efficiency was (104 ± 12)%. At potentials negative of the current spike, a $Ni(OH)_2{\cdot}xH_2O$ gel could constrain $H_2$ diffusion away from the gap between the two electrodes and thus form a local thin-layer cell.

**Local Potentiometric pH Measurements.** In preliminary measurements, the pH change in the diffusion layer during Ni deposition was examined (Figure 7). The Pt collector electrode in the SECM arrangement was modified using thin iridium oxide films to make potentiometric sensor probes. Details for fabrication of the pH probes and their calibration curves (Figure S14) are in the Supporting Information. The pH value at the potentiometric probe was calculated from measured potential values using the slope, (73 ± 2) mV/pH unit, of the calibration curves. The probe potential shifted by about −10 mV (less than one pH unit) at the onset of diffusion-limited $H_3O^+$ reduction on Au in NaCl as well as during Ni deposition in $NiCl_2$−NaCl electrolyte, indicating that negligible hydrolysis[62−64] of $Ni^{2+}$ occurs in this potential range

$$[Ni(H_2O)_6]^{2+} + H_2O \rightarrow [Ni(H_2O)_5(OH)]^{+} + H_3O^{+} \quad (4)$$

A sharp change of −20 mV appeared nearly coincident with the generator current spike at −1.27 V. However, as the generator potential was swept more negative, the increase in the rate of $H_2O$ reduction leads to a continuous rise in the pH of at least 7 orders of magnitude such that the pH of the diffusion layer exceeds 10 by −1.50 V, thus providing ample driving force for forming $Ni(OH)_2{\cdot}xH_2O$. Similar pH shifts were reported using a micrometer-sized grid electrode attached to a glass pH electrode.[6] On the basis of the $K_{sp}$ of $Ni(OH)_2$ (vide supra), saturation occurs above pH 8 in 5 mmol/L $Ni^{2+}$.

**Cyclic Voltammetry of 5 mmol/L $CoCl_2$ + 0.1 mol/L NaCl.** The generality of the UME observations was investigated with Co electrodeposition (Figure 8) because self-terminated metal deposition was reported for all iron group metals,[15] and cobalt hydroxide precipitation reportedly hindered Co deposition in other studies.[78] As the potential is swept negative, a small wave occurred at −0.78 V, corresponding to (3.5 ± 0.4) mC/cm$^2$, which is attributed to underpotential deposition (upd) of Co. The Co layer inhibits $H_3O^+$ reduction relative to Au. Between −0.9 and −1.1 V, the current associated with bulk $Co^{2+}$ and $H_3O^+$ reduction increased to transport-limited values. $D_{Co}$ was (7.3 ± 0.9) × 10$^{-6}$ cm$^2$/s, comparable with a literature value of 7.3 × 10$^{-6}$ cm$^2$/s.[59] The current efficiency determined using the steady-state current density at −1.20 V was (43 ± 3)%, and the integrated voltammetric current efficiency determined by comparing the reduction charge with that of

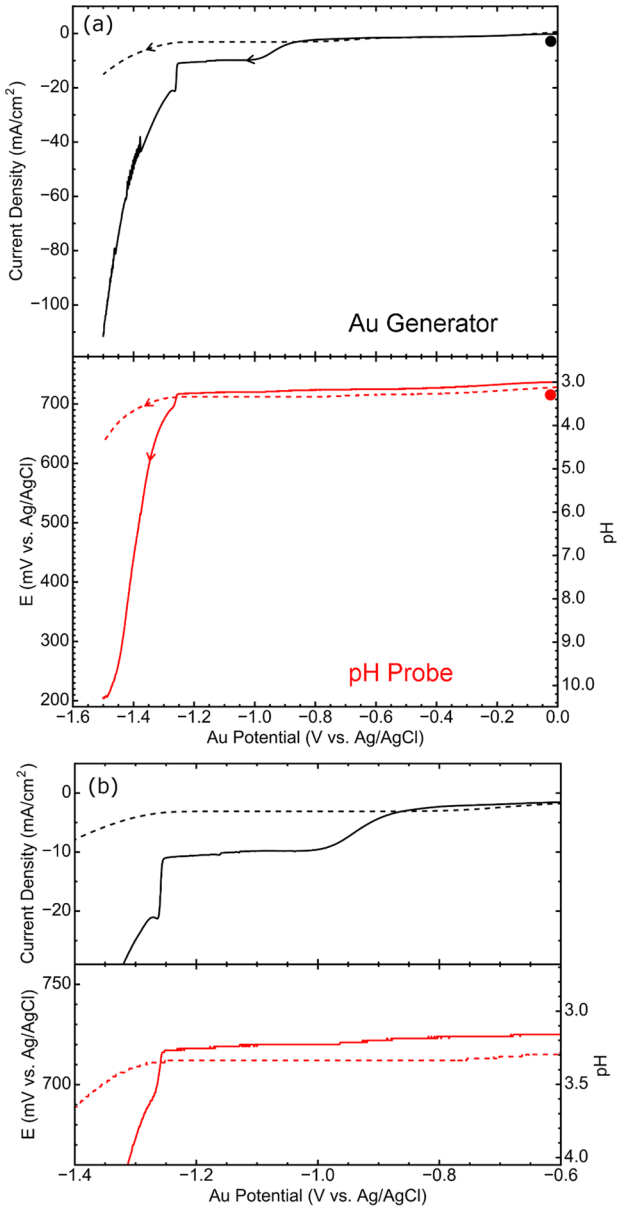


**Figure 7.** (a) Faradaic current (black) and pH probe potential and corresponding pH (red) as a function of Au ultramicroelectrode potential in 5.0 mmol/L $NiCl_2$ + 0.1 mol/L NaCl, pH 3.0. Dashed lines are in the supporting electrolyte. (b) Expanded view of features. Note that the range of both axes is different in panels a and b. Electrode separation, 12 μm; sweep rate, 10 mV/s; initial potential, 0.00 V; electrode radii, 12.5 μm. Experiments were done under ambient conditions.

the stripping peak was (56 ± 8)%. $H_2O$ reduction is evident near −1.4 V with a small current feature at −1.45 V (inset of Figure 8) that corresponds to potentials where self-termination of metal deposition was observed in EQCM measurements.[15] No clear current spike was observed, suggesting that Co/$Co(OH)_2$(ads) is less effective in catalyzing $H_2O$ reduction than Ni/$Ni(OH)_2$(ads), consistent with results comparing $Co(OH)_2$(ads) and $Ni(OH)_2$(ads) islands on Pt.[29] These results are also consistent with the conclusion that main current spike in $Ni^{2+}$ electrolytes is not due to simple hydrolysis (eq 4) because the p$K_a$ values, ≈10,[62] of $Co(OH)_2$ and $Ni(OH)_2$ are similar. On the reverse sweep, Co deposition was reactivated by −1.2 V, followed by a Co stripping wave at −0.21 V that was


DOI: 10.1021/acs.jpcc.6b10006
J. Phys. Chem. C XXXX, XXX, XXX−XXX

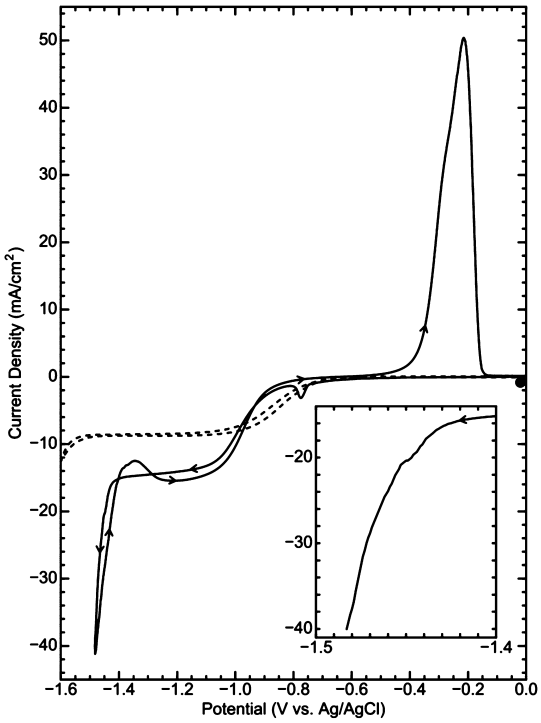


**Figure 8.** Cyclic voltammetry of Au ultramicroelectrode in 5.0 mmol/L $CoCl_2$ + 0.1 mol/L NaCl, pH 3.0. Inset shows expanded view of wave in current response near −1.45 V. Sweep rate, 20 mV/s; initial potential, 0.00 V; anodic potential limit, 0.00 V; electrode radius, 12.5 $\mu$m.

much larger than that for Ni stripping (Figure 1). In contrast to a $Ni(OH)_2$(ads) layer, $Co(OH)_2$(ads) provided little inhibition to reactivation of the deposition reaction at more positive potentials and as well as to subsequent Co dissolution at more positive potentials, in good agreement with the EQCM study[15] and results of others.[79]

## CONCLUSIONS

The well-defined mass transport conditions associated with UMEs provided several new insights into the electrodeposition of Ni on Au in $NiCl_2$−NaCl electrolytes. Voltammetry revealed an unusual sharp current spike coincident with the onset of $H_2O$ reduction and self-termination of Ni electrodeposition, and analysis of SECM measurements indicated that the spike is associated with $H_2$ evolution. These observations combined with recent reports of catalyzed $H_2O$ reduction at composite metal/$Ni(OH)_2$ electrodes suggests that the spike was due to autocatalytic $H_2$ production associated with $Ni(OH)_2$(ads) nucleation and growth on the Ni surface. Here, $OH^-$ generated via $H_2O$ reduction reacted with $Ni^{2+}$ to form a thin heterogeneous $Ni(OH)_2$(ads) layer. In a separate phenomenon, as the rate of $H_2O$ reduction increased at higher overpotentials, the pH increased such that the $K_{sp}$ of $Ni(OH)_2$ was exceeded and precipitation of a $Ni(OH)_2{\cdot}xH_2O$ gel occurred in the diffusion layer surrounding the UME. Regarding Ni deposition during concurrent $H_3O^+$ reduction, H may be incorporated in the growing Ni metal film, although other measurements would be needed to support this hypothesis. Studies are underway to couple voltammetry with in situ spectroscopy and to model quantitatively processes involved in both self-termination of the metal deposition reaction as well as the subsequent homogeneous precipitation in the diffusion layer.

## ASSOCIATED CONTENT

### Supporting Information

The Supporting Information is available free of charge on the ACS Publications website at DOI: 10.1021/acs.jpcc.6b10006.

CV of Au in $NiCl_2$−LiCl electrolyte, Pt in $NiCl_2$−NaCl electrolyte, Au in $NiCl_2$−$Na_2SO_4$ electrolyte, and Au in $NiCl_2$−NaCl−$H_3BO_3$ electrolyte; plot of $j$ vs $t^{-1/2}$ for current density immediately following current spike; voltammetry of Au in $NiCl_2$−NaCl electrolyte with potential poised at −1.20 V; CV of Au with varying radii in $NiCl_2$−NaCl electrolyte; voltammetry of Au in $NiCl_2$−NaCl electrolytes corresponding to Videos S1 and S2; processed images from Video S2; chronoamperometry of Au in $NiCl_2$−NaCl electrolytes; SEM and EDX images of electrodeposited Ni; Raman spectra of electrodeposited Ni; CV of Au/Ni in NaCl electrolyte; and calibration of pH probes (PDF)

Video S1: Optical microscopy measurements depicted in Figure 2a (AVI)

Video S2: Optical microscopy measurements depicted in Figure 2b (AVI)

Video S3: Optical microscopy measurements depicted in Figure 2c (AVI)

Video S4: Optical microscopy measurements depicted in Figure 2d (AVI)

Video S5: Optical microscopy measurements depicted in Figure 2e (AVI)

## AUTHOR INFORMATION

### Corresponding Authors

*E-mail: nicole.ritzert@nist.gov.

*E-mail: thomas.moffat@nist.gov.

### ORCID

Nicole L. Ritzert: 0000-0001-8680-6299

### Notes

The authors declare no competing financial interest.

## ACKNOWLEDGMENTS

N.L.R. acknowledges the National Institute of Standards and Technology-National Research Council research associateship program for a postdoctoral fellowship, Maureen Williams for performing SEM and EDX measurements, Carlos Beauchamp for assistance with the Summit camera, and the Center for Nanoscale Science and Technology for use of the Raman microscope.

## REFERENCES

(1) Dahms, H.; Croll, I. M. Anomalous Codeposition of Iron-Nickel Alloys. *J. Electrochem. Soc.* **1965**, *112*, 771−775.

(2) Harris, L. B. Change in pH near the Cathode during the Electrodeposition of a Bivalent Metal. Analysis. *J. Electrochem. Soc.* **1973**, *120*, 1034−1040.

(3) Fischer, W. Bildungsgeschwindigkeit von Nickelhydroxidschichten Während der Kathodischen Wasserstoffentwicklung. *Electrochim. Acta* **1976**, *21*, 1001−1007.

(4) Gómez, E.; Muller, C.; Proud, W. G.; Vallés, E. Electrodeposition of Nickel on Vitreous Carbon: Influence of Potential on Deposit Morphology. *J. Appl. Electrochem.* **1992**, *22*, 872−876.

(5) Vallés, E.; Pollina, R.; Gómez, E. Relation between the Presence of Inhibitors and Deposit Morphology in Nickel Deposition. *J. Appl. Electrochem.* **1993**, *23*, 508−515.



DOI: 10.1021/acs.jpcc.6b10006
J. Phys. Chem. C XXXX, XXX, XXX−XXX

(6) Deligianni, H.; Romankiw, L. T. *In situ* Surface pH Measurement during Electrolysis using a Rotating pH Electrode. *IBM J. Res. Dev.* **1993**, *37*, 85−95.
(7) Proud, W. G.; Muller, C. Electrodeposition of Nickel on Vitreous Carbon: Impedance Studies. *Electrochim. Acta* **1993**, *38*, 405−413.
(8) Cui, C. Q.; Lee, J. Y. Effects of Oxygen Reduction on Nickel Deposition from Unbuffered Aqueous Solutions. I. Deposition Process and Deposit Structure. *J. Electrochem. Soc.* **1994**, *141*, 2030−2035.
(9) Muñoz, A. G.; Salinas, D. R.; Bessone, J. B. First Stages of Ni Deposition onto Vitreous Carbon from Sulfate Solutions. *Thin Solid Films* **2003**, *429*, 119−128.
(10) Oriňaková, R.; Turoňová, A.; Kladeková, D.; Gálová, M.; Smith, R. M. Recent Developments in the Electrodeposition of Nickel and Some Nickel-Based Alloys. *J. Appl. Electrochem.* **2006**, *36*, 957−972.
(11) Song, S. Q.; Liu, Z.; Ortega, C. M.; Wu, W. S.; Sun, L. Electrochemical Study of Ni Deposition on Carbon Microfiber. *Electrochim. Acta* **2013**, *94*, 252−258.
(12) Zech, N.; Landolt, D. The Influence of Boric Acid and Sulfate Ions on the Hydrogen Formation in Ni-Fe Plating Electrolytes. *Electrochim. Acta* **2000**, *45*, 3461−3471.
(13) Motoyama, M.; Fukunaka, Y.; Sakka, T.; Ogata, Y. H. Effect of Surface pH on Electrodeposited Ni Films. *J. Electrochem. Soc.* **2006**, *153*, C502−C508.
(14) Vazquez-Arenas, J.; Altamirano-Garcia, L.; Pritzker, M.; Luna-Sánchez, R.; Cabrera-Sierra, R. Experimental and Modeling Study of Nickel Electrodeposition Including $H^+$ and Water Reduction and Homogeneous Reactions. *J. Electrochem. Soc.* **2011**, *158*, D33−D41.
(15) Wang, R.; Bertocci, U.; Tan, H.; Bendersky, L. A.; Moffat, T. P. Self-Terminated Electrodeposition of Ni, Co, and Fe Ultrathin Films. *J. Phys. Chem. C* **2016**, *120*, 16228−16237.
(16) Vanpaemel, J.; van der Veen, M. H.; De Gendt, S.; Vereecken, P. M. Enhanced Nucleation of Ni Nanoparticles on TiN through $H_3BO_3$ Mediated Limited Growth. *Electrochim. Acta* **2013**, *109*, 411−418.
(17) Vanpaemel, J.; Sugiura, M.; Cuypers, D.; van der Veen, M. H.; De Gendt, S.; Vereecken, P. M. Electrochemical Deposition of Subnanometer Ni Films on TiN. *Langmuir* **2014**, *30*, 2047−2053.
(18) Streinz, C. C.; Hartman, A. P.; Motupally, S.; Weidner, J. W. Effect of Current and Nickel Nitrate Concentration on the Deposition of Nickel Hydroxide Films. *J. Electrochem. Soc.* **1995**, *142*, 1084−1089.
(19) Doyle, R. L.; Godwin, I. J.; Brandon, M. P.; Lyons, M. E. G. Redox and Electrochemical Water Splitting Catalytic Properties of Hydrated Metal Oxide Modified Electrodes. *Phys. Chem. Chem. Phys.* **2013**, *15*, 13737−13783.
(20) Hall, D. S.; Lockwood, D. J.; Bock, C.; MacDougall, B. R. Nickel Hydroxides and Related Materials: A Review of Their Structures, Synthesis, and Properties. *Proc. R. Soc. London, Ser. A* **2015**, *471*, 20140792.
(21) Dionigi, F.; Strasser, P. NiFe-Based (Oxy)hydroxide Catalysts for Oxygen Evolution Reaction in Non-Acidic Electrolytes. *Adv. Energy Mater.* **2016**, 1600621.
(22) Beck, F.; Rüetschi, P. Rechargeable Batteries with Aqueous Electrolytes. *Electrochim. Acta* **2000**, *45*, 2467−2482.
(23) Diaz-Morales, O.; Ledezma-Yanez, I.; Koper, M. T. M.; Calle-Vallejo, F. Guidelines for the Rational Design of Ni-Based Double Hydroxide Electrocatalysts for the Oxygen Evolution Reaction. *ACS Catal.* **2015**, *5*, 5380−5387.
(24) Wang, H.; Casalongue, H. S.; Liang, Y.; Dai, H. $Ni(OH)_2$ Nanoplatelets Grown on Graphene as Advanced Electrochemical Pseudocapacitor Materials. *J. Am. Chem. Soc.* **2010**, *132*, 7472−7477.
(25) Zhu, Y.; Cao, C.; Tao, S.; Chu, W.; Wu, Z.; Li, Y. Ultrathin Nickel Hydroxide and Oxide Nanosheets: Synthesis, Characterizations and Excellent Supercapacitor Performances. *Sci. Rep.* **2014**, *4*, 5787.
(26) E, S. P.; Liu, D.; Lazenby, R. A.; Sloan, J.; Vidotti, M.; Unwin, P. R.; Macpherson, J. V. Electrodeposition of Nickel Hydroxide Nanoparticles on Carbon Nanotube Electrodes: Correlation of Particle Crystallography with Electrocatalytic Properties. *J. Phys. Chem. C* **2016**, *120*, 16059−16068.
(27) Subbaraman, R.; Tripkovic, D.; Strmcnik, D.; Chang, K.-C.; Uchimura, M.; Paulikas, A. P.; Stamenkovic, V.; Markovic, N. Enhancing Hydrogen Evolution Activity in Water Splitting by Tailoring $Li^+$-$Ni(OH)_2$-Pt Interfaces. *Science* **2011**, *334*, 1256−1260.
(28) Danilovic, N.; Subbaraman, R.; Strmcnik, D.; Chang, K. C.; Paulikas, A. P.; Stamenkovic, V. R.; Markovic, N. M. Enhancing the Alkaline Hydrogen Evolution Reaction Activity through the Bifunctionality of $Ni(OH)_2$/Metal Catalysts. *Angew. Chem., Int. Ed.* **2012**, *51*, 12495−12498.
(29) Subbaraman, R.; Tripkovic, D.; Chang, K.-C.; Strmcnik, D.; Paulikas, A. P.; Hirunsit, P.; Chan, M.; Greeley, J.; Stamenkovic, V.; Markovic, N. M. Trends in Activity for the Water Electrolyzer on 3d M(Ni, Co, Fe, Mn) Hydr(oxy)oxide Catalysts. *Nat. Mater.* **2012**, *11*, 550−557.
(30) Wightman, R. M. Microvoltammetric Electrodes. *Anal. Chem.* **1981**, *53*, 1125A−1134A.
(31) Fleischmann, M.; Pons, S. The Behavior of Microelectrodes. *Anal. Chem.* **1987**, *59*, 1391A−1399A.
(32) Pletcher, D. Studies of Metal Deposition and Dissolution using Microelectrodes. In *Microelectrodes: Theory and Applications*; Montenegro, M. I., Quierós, M. A., Daschbach, J. L., Eds.; Kluwer Academic: Netherlands, 1991; pp 463−475.
(33) Heinze, J. Ultramicroelectrodes in Electrochemistry. *Angew. Chem., Int. Ed. Engl.* **1993**, *32*, 1268−1288.
(34) Gibbs-Davis, J. M.; Kruk, J. J.; Konek, C. T.; Scheidt, K. A.; Geiger, F. M. Jammed Acid-Base Reactions at Interfaces. *J. Am. Chem. Soc.* **2008**, *130*, 15444−15447.
(35) Lis, D.; Backus, E. H. G.; Hunger, J.; Parekh, S. H.; Bonn, M. Liquid Flow along a Solid Surface Reversibly Alters Interfacial Chemistry. *Science* **2014**, *344*, 1138−1142.
(36) Scharifker, B.; Hills, G. Electrochemical Kinetics at Microscopically Small Electrodes. *J. Electroanal. Chem. Interfacial Electrochem.* **1981**, *130*, 81−97.
(37) John, R.; Wallace, G. G. The Use of Microelectrodes to Probe the Electropolymerization Mechanism of Heterocyclic Conducting Polymers. *J. Electroanal. Chem. Interfacial Electrochem.* **1991**, *306*, 157−167.
(38) Bade, K.; Tsakova, V.; Schultze, J. W. Nucleation, Growth, and Branching of Polyaniline from Microelectrode Experiments. *Electrochim. Acta* **1992**, *37*, 2255−2261.
(39) Chen, S.; Kucernak, A. Electrodeposition on Nanometer-Sized Carbon Electrodes. *J. Phys. Chem. B* **2003**, *107*, 8392−8402.
(40) Petrović, Ž.; Metikoš-Huković, M.; Grubać, Z.; Omanović, S. The Nucleation of Ni on Carbon Microelectrodes and Its Electrocatalytic Activity in Hydrogen Evolution. *Thin Solid Films* **2006**, *513*, 193−200.
(41) Eguiluz, K. I. B.; Avaca, L. A.; Barin, C. S. Estudo da Electrocristalização de Ni e Ni-P sobre Ultramicroelectrodes de Platina. *Quim. Nova* **2008**, *31*, 1150−1155.
(42) Velmurugan, J.; Noël, J.-M.; Nogala, W.; Mirkin, M. V. Nucleation and Growth of Metal on Nanoelectrodes. *Chem. Sci.* **2012**, *3*, 3307−3314.
(43) Schilardi, P. L.; Marchiano, S. L.; Salvarezza, R. C.; Hernandez Creus, A.; Arvia, A. J. Kinetics and Growth Modes of Quasi-2d Silver Branched Electrodeposits Produced in the Presence of a Supporting Electrolyte. *J. Electroanal. Chem.* **1997**, *431*, 81−98.
(44) Mauzeroll, J.; Hueske, E. A.; Bard, A. J. Scanning Electrochemical Microscopy. 48. Hg/Pt Hemispherical Ultramicroelectrodes: Fabrication and Characterization. *Anal. Chem.* **2003**, *75*, 3880−3889.
(45) Hammadi, Z.; Astier, J.-P.; Morin, R.; Veesler, S. Protein Crystallization Induced by a Localized Voltage. *Cryst. Growth Des.* **2007**, *7*, 1472−1475.
(46) Birkin, P. R.; Nestoridi, M.; Pletcher, D. Studies of the Anodic Dissolution of Aluminum Alloys Containing Tin and Gallium using Imaging with a High-Speed Camera. *Electrochim. Acta* **2009**, *54*, 6668−6673.
(47) Jebaraj, A. J. J.; Scherson, D. A. Microparticle Electrodes and Single Particle Microbatteries: Electrochemical and in Situ MicroRaman Spectroscopic Studies. *Acc. Chem. Res.* **2013**, *46*, 1192−1205.


DOI: 10.1021/acs.jpcc.6b10006
J. Phys. Chem. C XXXX, XXX, XXX−XXX

(48) Bard, A. J.; Fan, F.-R. F.; Kwak, J.; Lev, O. Scanning Electrochemical Microscopy. Introduction and Principles. *Anal. Chem.* **1989**, *61*, 132−138.
(49) Zhou, F.; Unwin, P. R.; Bard, A. J. Scanning Electrochemical Microscopy. 16. Study of Second-Order Homogeneous Chemical Reactions via the Feedback and Generation/Collection Modes. *J. Phys. Chem.* **1992**, *96*, 4917−4924.
(50) Sánchez-Sánchez, C. M.; Rodríguez-López, J.; Bard, A. J. Scanning Electrochemical Microscopy. 60. Quantitative Calibration of the SECM Substrate Generation/Tip Collection Mode and Its Use for the Study of the Oxygen Reduction Mechanism. *Anal. Chem.* **2008**, *80*, 3254−3260.
(51) Bard, A. J.; Fan, F.-R; Mirkin, M. V. Scanning Electrochemical Microscopy. In *Electroanalytical Chemistry: A Series of Advances*; Marcel Dekker: New York, 1994; Vol. *18*, pp 243−373.
(52) Mirkin, M. V.; Wang, Y. Theory. In *Scanning Electrochemical Microscopy*, 2nd ed., Bard, A. J., Mirkin, M. V., Eds.; CRC Press: Boca Raton, FL, 2012; pp 75−125.
(53) Bertocci, U.; Wagman, D. D. Copper, Silver, and Gold. In *Standard Potentials in Aqueous Solution*; Bard, A. J., Parsons, R., Jordan, J., Eds.; Marcel Dekker: New York, 1985; pp 287−320.
(54) Rasband, W. S. ImageJ. http://imagej.nih.gov/ij/ (accessed June 6, 2016).
(55) Deltombe, E.; de Zoubov, N.; Pourbaix, M. Nickel. In *Atlas of Electrochemical Equilibria in Aqueous Solutions*, 2nd ed.; National Association of Corrosion Engineers: Houston, TX, 1974; pp 330−342.
(56) Ji, J.; Cooper, W. C. Nickel Speciation in Aqueous Chloride Solutions. *Electrochim. Acta* **1996**, *41*, 1549−1560.
(57) Bard, A. J.; Faulkner, L. R. *Electrochemical Methods: Fundamentals and Applications*, 2nd ed.; Wiley: New York, 2001.
(58) Ariva, A. J.; Posadas, D. Nickel, Palladium, and Platinum. In *Standard Potentials in Aqueous Solution*; Bard, A. J., Parsons, R., Jordan, J., Eds.; Marcel Dekker: New York, 1985; pp 321−365.
(59) Vanysek, P. Ionic Conductivity and Diffusion at Infinite Dilution. In *CRC Handbook of Chemistry and Physics*, 97th ed.; Haynes, W. M., Ed.; CRC Press/Taylor and Francis: Boca Raton, FL, Internet Version 2017.
(60) Harrison, J. A.; Thirsk, H. R. Fundamentals of Metal Deposition. In *Electroanalytical Chemistry: A Series of Advances*; Marcel Dekker: New York, 1971; Vol. *5*, pp 67−148.
(61) Auinger, M.; Katsounaros, I.; Meier, J. C.; Klemm, S. O.; Biedermann, R. U.; Topalov, A. A.; Rohwerder, M.; Mayrhofer, K. J. J. Near-surface Ion Distribution and Buffer Effects during Electrochemical Reactions. *Phys. Chem. Chem. Phys.* **2011**, *13*, 16384−16394.
(62) Baes, C. F.; Mesmer, R. E. *Hydrolysis of Cations*; John Wiley: New York, 1976.
(63) Burgess, J. *Metal Ions in Solution*; Ellis Horwood: Chichester, Sussex, England, 1978.
(64) Grégoire, B.; Ruby, C.; Carteret, C. Hydrolysis of Mixed $Ni^{2+}$-$Fe^{3+}$ and $Mg^{2+}$-$Fe^{3+}$ Solutions and Mechanism of Formation of Layered Double Hydroxides. *Dalton Trans.* **2013**, *42*, 15687−15698.
(65) Harris, D. C. *Quantitative Chemical Analysis*, 5th ed.; W. H. Freeman: New York, 1999.
(66) Stevenson, K. J.; Hatchett, D. W.; White, H. S. Electrochemical Deposition of Polyborate Monolayers at Ag(111) Electrodes. *Langmuir* **1997**, *13*, 6824−6828.
(67) Dayton, M. A.; Ewing, A. G.; Wightman, R. M. Response of Microvoltammetic Electrodes to Homogeneous Catalytic and Slow Heterogeneous Charge-Transfer Reactions. *Anal. Chem.* **1980**, *52*, 2392−2396.
(68) Dayton, M. A.; Brown, J. C.; Stutts, K. J.; Wightman, R. M. Faradaic Electrochemistry at Microvoltammetric Electrodes. *Anal. Chem.* **1980**, *52*, 946−950.
(69) Desilvestro, J.; Corrigan, D. A.; Weaver, M. J. Characterization of Redox States of Nickel Hydroxide Film Electrodes by *In Situ* Surface Raman Spectroscopy. *J. Electrochem. Soc.* **1988**, *135*, 885−892.
(70) Chambers, W.; Fellers, T. J.; Davidson, M. W. Darkfield Illumination. http://www.microscopyu.com/articles/stereomicroscopy/stereodarkfield.html (accessed July 14, 2016).
(71) Howarth, J. N.; Pletcher, D. The Electrodeposition of Chromium from Chromium (III) Solutions-A Study using Microelectrodes. *J. Appl. Electrochem.* **1988**, *18*, 644−652.
(72) Luo, L.; White, H. S. Electrogeneration of Single Nanobubbles at Sub-50-nm-Radius Platinum Nanodisk Electrodes. *Langmuir* **2013**, *29*, 11169−11175.
(73) Lupo, C.; Stumpp, M.; Schlettwein, D. Diffusion-controlled Electrochemical Growth of Porous Zinc Oxide on Microstructured Electrode Band Arrays. *J. Appl. Electrochem.* **2015**, *45*, 105−113.
(74) Kim, J.; Yoon, S.-H. Failure Mechanism of a Gold Microelectrode in Bioelectronics applications. *J. Nanomater.* **2015**, *2015*, 1−7.
(75) Sauter, S.; Wittstock, G. Local Deposition and Characterization of $K_2Co[Fe(CN)_6]$ and $K_2Ni[Fe(CN)_6]$ by Scanning Electrochemical Microscopy. *J. Solid State Electrochem.* **2001**, *5*, 205−211.
(76) Hall, D. S.; Lockwood, D. J.; Poirier, S.; Bock, C.; MacDougall, B. R. Raman and Infrared Spectroscopy of $\alpha$ and $\beta$ Phases of Thin Nickel Hydroxide Films Electrochemically Formed on Nickel. *J. Phys. Chem. A* **2012**, *116*, 6771−6784 and references therein..
(77) Solla-Gullón, J.; Aldaz, A.; Clavilier, J. Ultra-Low Platinum Coverage at Gold Electrodes and Its Effect on the Hydrogen Evolution Reaction in Acidic Solutions. *Electrochim. Acta* **2013**, *87*, 669−675.
(78) Mech, K.; Zabinski, P.; Kowalik, R. Co-Reduction of Electrochemically Active $[Co(H_2O)_6]^{2+}$ and $[CoCl(H_2O)_5]^{+}$ Complexes onto Gold Electrode. *J. Electrochem. Soc.* **2013**, *160*, D246−D250.
(79) Allongue, P.; Maroun, F. Electrodeposited Magnetic Layers in the Ultrathin Limit. *MRS Bull.* **2010**, *35*, 761−770.


DOI: 10.1021/acs.jpcc.6b10006
J. Phys. Chem. C XXXX, XXX, XXX−XXX